Management of the axial modulation of the illumination pattern in structured illumination microscopy using an extended illumination source

ALEJANDRO GIMENO-GOMEZ,[1] SEYEDEH PARISA DAJKHOSH,[2] CONG TUAN SON VAN,[2] JUAN CARLOS BARREIRO,[1] CHRYSANTHE PREZA,[2,3] AND GENARO SAAVEDRA[1,4] (ID)

[1]*3D Imaging & Display Laboratory, Universitat de València, Burjassot, Spain*
[2]*Computational Imaging Research Laboratory, Dept. of Electrical & Computer Engineering, University of Memphis, Memphis, TN, USA*
[3]*cpreza@memphis.edu*
[4]*genaro.saavedra@uv.es*

Abstract: We have designed and implemented an approach for three-dimensional (3D) structured illumination (SI) microscopy (SIM) based on a quasi-monochromatic extended source illuminating a Wollaston prism to improve robustness, light efficiency and flexibility over our previous design. We show through analytical and experimental verification of the presented theoretical framework for our proposed tunable structured illumination microscopy (TSIM) system, that a simple and accurate determination of the axial modulation of the SI pattern is achieved, enabling a realistic characterization of the system's effective optical transfer function (OTF). System performance as a function of the extended source size is investigated with simulations. Results from a comparative performance analysis of the proposed TSIM system and traditional SIM systems show some advantages over the traditional two-wave and three-wave interference SIM systems. We show that by controlling the source size and thereby the axial modulation of the 3D SI pattern, the TSIM scheme offers increased OTF compact support and improved optical sectioning capability, quantified by the integrated intensity, under certain conditions, which may be desirable when imaging optically thick samples. The additional tunability of the 3D SI pattern, provides a unique opportunity for OTF engineering in our TSIM system.

1. Introduction

The use of non-uniform irradiance patterns has been widely used as a way for improving the performance of inspection systems in combination with digital post processing. In particular, structured illumination (SI) microscopy (SIM) is based on the non-uniform illumination of three-dimensional (3D) samples to overcome the known imaging limitations of widefield fluorescence microscopy (WFM), such as lack of optical sectioning and limited resolution due to diffraction [1,2].

   The simplest approach is to use a non-diffracting beam as an illumination pattern, as the one obtained typically after two plane-wave interference (2WSIM). The symmetrical layout leads in this case to an axially invariant illumination with a single lateral spatial frequency [1]. This approach presents some trade-offs between the lateral and axial SIM system performance [3,4] that led to the introduction of other irradiation schemes based on three plane-wave interference (3WSIM) [2], by adding more lateral frequencies that generate both axial and lateral variation of the illumination pattern (3D-SIM by 3WSIM). However, the use of more than one lateral modulation frequency adds complexity to the data post-processing of the recorded raw images, increasing at

the same time the minimum number of images required for the accurate reconstruction of the 3D structure of the sample (see [5] and references therein). Note that all these approaches make use of a one-dimensional (1D) transverse illumination pattern that has to be rotated twice in repeated through-focus (axial) steps during data-acquisition to achieve isotropic lateral super-resolution. Instead, in lattice SIM, the illumination system directly projects transverse two-dimensional (2D) periodic patterns onto the sample, ideally improving light efficiency and signal-to-noise ratio [6–8]. These 2D SI patterns are generated typically by either interference of four or more mutually coherent plane waves [7] or by use of customized diffractive optical elements (see [9] and references therein). However, in any case, some drawbacks are still pending to overcome in the lattice SIM approach, such as coherent noise disturbance and even a greater number of captured images needed for an accurate reconstruction of a 3D sample compared to the other 3D-SIM approaches.

Although the first proposals in 3D-SIM were essentially based on coherent illumination, incoherent sources are currently widely used to increase the signal-to-noise ratio of the final reconstructions. Even in the pioneering papers by Gustafsson et al. [1,2], a limited breaking of the spatial coherence in illumination was proposed to reduce coherent noise. However, the most extended implementation of SIM by using spatially incoherent illumination is based on the projection of an incoherently irradiated 1D grating onto the sample space [10]. This approach has been proven to be very efficient in providing optical-sectioning capability in 3D imaging, due to the narrow axial confinement of the modulation illumination pattern that is generated and projected on the sample. Nevertheless, this approach does not provide a relevant improvement in lateral resolution over WFM because the image of the projected grating is filtered out by the optical transfer function (OTF) of the illumination system of the microscope, and thus a dramatic decrease in the contrast of the projected pattern happens when modulation frequencies that could lead to significant lateral super resolution are used. Recently, we proposed a different method to axially modulate a single lateral-frequency pattern by using a tailored spatially incoherent source, consisting of an array of parallel equidistant slits, illuminating a Fresnel biprism [11]. In our proposal, the incoherent source is not projected onto the focused plane of the sample, but onto the pupil plane of the illumination system. The induced axial variation is straightforwardly transmitted to the effective OTF of the computational optical system required for the proper recovery of the 3D object's intensity. Our approach provides a reduction in both the number of required raw images and in the complexity of the 3D reconstruction process, compared to the 3WSIM approach [2]. The 3D illumination pattern generated with this approach provides lateral and axial periodic variations, with frequencies that can be independently and continuously tuned, by simply axially shifting the position of the Fresnel biprism and/or changing the slit separation. This decoupling in the axial and lateral modulation frequencies of the 3D SI pattern allows further design of the compact support of the OTF [12].

Although our original proposal was based on the use of a Fresnel biprism, further research led us to move to a more convenient refractive element: a Wollaston prism, which offers several advantages [13–15]. First, diffraction at the edges of these elements generates a transverse envelope of the ideal cosinusoidal pattern considered in conventional SIM approaches. This extra modulation is much flatter in the case of the Wollaston prism [13]. Second, due to the prism size limitation, an axial variation of the field of view (FoV) of the SI pattern is obtained. Simultaneously, an extra axial modulation of the visibility of the cosinusoidal pattern appears. In the case of the Fresnel prism, the maximum visibility plane corresponds to the minimum attainable FoV [16], while when using the Wollaston prism, maximum values of both FoV and visibility are obtained at the prism plane. Finally, the Wollaston prism adds an extra degree of freedom to the control of the SI pattern, namely, polarization. A de Senarmont compensator scheme has been used advantageously, in fact, in our latest implementations to introduce the phase shift required in the raw SIM images [14,15].

In this work we propose an approach based on the use of a general extended source illuminating a Wollaston prism. We present here a theoretical framework and a experimental validation for the effect of an arbitrary shape of the incoherent source on the illumination pattern, by showing the mathematical relationship between the spatial structure of the irradiance distribution of the source and the axial modulation of the visibility of the periodic transverse pattern projected in the sample space. Physically, each of the source points is split into two mutually coherent emitters, that interfere and generate a cosinusoidal pattern. By incoherently adding the contribution of the whole set of points in the source, a resulting cosinusoidal pattern is obtained whose visibility changes from plane to plane. Thus, the 3D illumination pattern generated with this approach is axially varying based on the shape of the source, while it simultaneously provides lateral periodic variations, which can be tuned by simply axially shifting the position of the Wollaston prism. With respect to our previous proposal, which used an array of equidistant incoherent linear sources, the novel architecture proposed here provides in general a much higher light throughput (significantly more light from an extended source than through the slit array), increased flexibility in the implementation (no need to fabricate slit array elements for different designs), decreased mechanical alignment requirements and improved signal-to-noise ratio performance.

Results presented in this contribution provide a practical method for obtaining a better approach to determine a more realistic axially modulated PSF or OTF that can be used in the digital image reconstruction of 3D samples, ideally providing a reduction in possible computational artifacts. Furthermore, this approach provides the possibility for an extra tunability of the 3D-SIM technique, since by controlling the shape of the illumination source, some particular features of the OTF can be reinforced or diminished providing an additional flexibility to potentially fit the imaging system to particular goals in inspection techniques.

2. Theory

In this section, we obtain the mathematical expression for the SI pattern in our proposed approach. Supplement 1 provides some background information about patterns generated by a Wollaston prism under coherent illumination. From these results, we show next how we use the Wollaston prism to generate our tunable SI based on an extended quasimonochromatic source with an arbitrary shape.

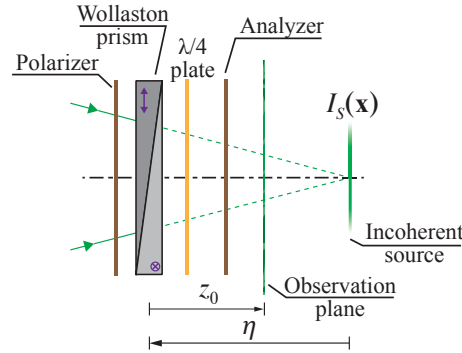### 2.1. Incoherent Wollaston-prism-based illumination generator using an extended planar source

Let us consider now that the setup introduced in Supplement 1 is illuminated by an extended, planar quasimonochromatic source located at a distance η, as indicated in Fig. 1. The total radiant power of the source will be denoted as P. Note that $\eta<0$ in the figure, but $\eta>0$ is also included in our reasoning.

From a physical point of view, when using an extended quasimonochromatic source, the irradiance distribution at any observation transverse plane can be described as an incoherent superposition of the irradiance patterns generated by each of the source points separately. In our case, each elemental emitter creates the same cosinusoidal pattern as given in Eq. (S3), but laterally shifted according to its projection through the axial point of the Wollaston prism onto the observation plane. In general, the superposition of such off-set identical distributions produces a cosinusoidal pattern with reduced visibility, whose particular value depends on the spatial distribution of the source irradiance and the relative distances in the above-mentioned projection. Thus, an axial modulation of the visibility of the transverse irradiance patterns is generated. Mathematically, within the Fresnel approximation, the irradiance distribution on a

transverse plane at a distance z_0 from the prism is given by [17]

$$I_0(\mathbf{x}, z_0) = \left(-\frac{\eta}{z_0}\right)^2 P\, I_S\left(-\frac{\eta}{z_0}\mathbf{x}\right) \otimes_2 \bar{I}_0(\mathbf{x}, z_0)\,, \tag{1}$$

where $I_S(\mathbf{x})$ stands for the irradiance distribution of the source normalized to have unity area, and $\otimes_2$ is the 2D convolution operation with respect to the lateral coordinates $\mathbf{x} = (x, y)$. In the equation above $\bar{I}_0(x, z_0)$ stands for the diffraction pattern of the object when an axial point source is used, i.e., the result in Eq. (S3). Note that this result considers the coherent superposition of light coming from the two replicas of each point onto the source plane generated by the Wollaston prism, following an incoherent superposition for all points from the source. In fact, the irradiance distribution generated onto the source plane after considering the Wollaston prism effect consists of two replicas of the original irradiance distribution separated by a distance $2a$ given by Eq. (S2), but with points that are mutually coherent in pairs.

Fig. 1. Sketch of the Wollaston-prism-based setup when illuminated by an extended spatially incoherent source.

By substituting the result in Eq. (S3) in Eq. (1), one can find that the irradiance distribution after considering the whole set of incoherent points of the source can be expressed as

$$I_0(\mathbf{x}, z_0) = 1 + |V_0(z_0)| \cos\left[2\pi\mathbf{u}_0(z_0) \cdot \mathbf{x} + \phi + \Phi_0(z_0)\right]\,, \tag{2}$$

with the axial variation of the complex visibility of the pattern given by

$$V_0(z_0) = \tilde{I}_S\left(\frac{-z_0\mathbf{u}_0(z_0)}{\eta}\right)\,, \tag{3}$$

where $\tilde{I}_S(\mathbf{u}) = \mathcal{F}_{2D}\{I_S(\mathbf{x}); \mathbf{u}\}$ is the 2D Fourier transform of the normalized irradiance distribution of the source, being $\mathbf{u} = (u, v)$ the lateral 2D spatial frequency. In Eq. (2) the phase shifting function $\Phi_0(z_0)$ stands for the argument of the complex visibility $V_0(z_0)$. Both the spatial frequency $\mathbf{u}_0(z_0)$ and the lateral phase shift ϕ are defined in Suplement 1.

Note here the explicit dependence of the lateral frequency of the diffraction pattern with the propagation distance z_0, which is rather incovenient for the standard reconstruction algorithms used in SIM. To obtain a fixed single lateral period for any transverse plane, we consider now a collimating scheme in which an ideal lens with focal length f_c is located with its front focal plane onto the extended source. Neglecting the effects of the finite size of the lens, the new irradiance patterns can be obtained as images of the respective ones according to the laws of geometrical optics. Thus, the irradiance pattern obtained after the effect of the lens at a distance z_c of the

image of the Wollaston prism can be computed as

$$I_c(\mathbf{x}, z_c) = I_0\left(\frac{\mathbf{x}}{M_c(z_0)}, z_0\right) \, , \tag{4}$$

where, according to geometrical optics' equations for conjugate distances [18], the following relationships hold

$$z_c = -\frac{f_c^2}{z_0 + \eta} - t \, , \text{ and}$$

$$M_c(z_0) = \frac{f_c}{z_0 + \eta} \, , \tag{5}$$

$t = -f_c^2/\eta$ being the distance from the back focal plane of the lens to the image of the Wollaston prism (see Fig. 2). These equations link the transverse patterns after the collimation lens, $I_c(\mathbf{x}, z_c)$, and their counterparts before the actuation of this lens, $I_0(\mathbf{x}, z_0)$. Thus, now the irradiance pattern at a distance z_c from the image of the Wollaston prism is a scaled version (with magnification $M_c(z_0)$) of the previous irradiance distribution at a distance z_0 from the Wollaston prism. By using these relationships in Eq. (4), one can obtain

$$I_c(\mathbf{x}, z_c) = 1 + |V_c(z_c)| \cos\left[2\pi\mathbf{u}_0' \cdot \mathbf{x} + \phi + \Phi_c(z_c)\right] \, , \tag{6}$$
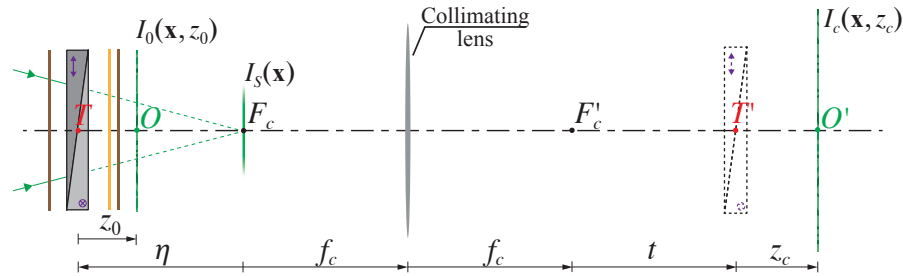
where

$$\mathbf{u}_0' = \frac{\mathbf{u}_0(z_0)}{M_c(z_0)} = \frac{\eta}{f_c}\mathbf{u}_W \, , \tag{7}$$

is the new constant lateral frequency of the pattern (see Suplement 1 for definition of $\mathbf{u}_W$) and where the axial modulation of the visibility is now given by

$$V_c(z_c) = \tilde{I}_S\left(\frac{-z_c\mathbf{u}_0'}{f_c}\right) = \tilde{I}_S\left(\frac{-z_c\eta}{f_c^2}\mathbf{u}_W\right) \, . \tag{8}$$

Again the function $\Phi_c(z_c)$ is the argument of the above complex visibility.

Fig. 2. Scheme of the collimated configuration of the proposed illumination system. T' and O' represent, respectively, the image of the axial points T (Wollaston prism) and O (transverse observation plane) by the collimating lens.

Note that, after the collimation, the irradiance patterns present a single lateral frequency $\mathbf{u}_0'$ that can be continuously tuned by changing the distance η. In practice, axial shifting of the prism can be used for achieving this change. On the other hand, since the source irradiance function $I_S(\mathbf{x})$ is a real positive function, $|V_c(z_c)|$ is maximum at $z_c = 0$. This means that the conjugate plane of the prism formed by the collimating lens is a maximum contrast plane, independently of the particular source used.

Finally, the 3D irradiance pattern described in Eq. (6) should be properly projected onto the sample space to generate a structured illumination on the specimen. To preserve a single lateral

frequency for the actual illumination of the sample, a telecentric projection relay should be considered. It is straightforward to find then that the illumination pattern finally projected is given by

$$S(\mathbf{x}, z) = I_c \left(\frac{\mathbf{x}}{M_{ill}}, z_c \right) , \tag{9}$$

where $z = nM_{ill}^2 z_c$, M_{ill} standing for the lateral magnification of the projection relay, and n being the refractive index of the immersion medium. After mathematical manipulation, it is obtained

$$S(\mathbf{x}, z) = 1 + |V(z)| \cos \left[2\pi \mathbf{u}_m \cdot \mathbf{x} + \phi + \Phi(z) \right] , \tag{10}$$

z being the distance from the image of the Wollaston prism onto the sample space, and where

$$V(z) = V_c \left(\frac{z}{nM_{ill}^2} \right) = \tilde{I}_S \left(\frac{-z\eta}{nM_{ill}^2 f_c^2} \mathbf{u}_W \right) = \tilde{I}_S \left(\frac{-z}{nM_{ill} f_c} \mathbf{u}_m \right) , \tag{11}$$

and the lateral modulation frequency is

$$\mathbf{u}_m = \frac{\mathbf{u}_0'}{M_{ill}} = \frac{\eta}{M_{ill} f_c} \mathbf{u}_W = u_m \hat{\mathbf{s}}_W . \tag{12}$$

In the above equations, $\Phi(z)$ is the complex argument of $V(z)$. Equation (11) provides the axial modulation of the visibility of the single-lateral-frequency patterns generated from a given shape $I_S(\mathbf{x})$ for the irradiance of the source used in the setup. According to this equation, a scaled 2D Fourier transform of $I_S(\mathbf{x})$ has to be performed and the corresponding central profile along the $\hat{\mathbf{s}}_W$ direction provides the values of $V(z)$. However, according to the *central slice theorem*[19], the same result is obtained by projecting the 2D function $I_S(\mathbf{x})$ onto a line parallel to $\hat{\mathbf{s}}_W$ and then taking a 1D Fourier transform. Mathematically,

$$V(z) = \mathcal{F}_{1D} \left\{ \Pi_{\hat{\mathbf{s}}_W} \left\{ I_S(\mathbf{x}); \zeta \right\} ; \frac{-z u_m}{n M_{ill} f_c} \right\} , \tag{13}$$

where

$$\Pi_{\hat{\mathbf{s}}_W} \left\{ I_S(\mathbf{x}); \zeta \right\} = \iint I_S(\mathbf{x}) \delta(\zeta - \mathbf{x} \cdot \hat{\mathbf{s}}_W) d^2\mathbf{x} , \tag{14}$$

$\delta(\zeta)$ being the Dirac delta function. Figure 3 summarizes the operations connecting the irradiance of the source and the axial modulation of the visibility of the structured illumination patterns generated into the sample. Note that, according to Eq. (13), the complex visibility $V(z)$ is a Hermitian function, i.e, $V^*(-z) = V(z)$, since it is obtained as the Fourier transform of a real-valued function ($\Pi_{\hat{\mathbf{s}}_W} \left\{ I_S(\mathbf{x}); \zeta \right\}$). This property also leads to a symmetric $|V(z)|$ distribution.

From a practical point of view, one may think that the effect of the OTF of the projection system has to be included in this reasoning, affecting the result in Eq. (13). However, we prove next that is not the case. If we fix our attention in the typical epi-illumination scheme, the illumination relay is composed of an illumination tube lens TL_1, with a focal length f_{TL1}, and the microscope objective itself (see Fig. 4). Since before TL_1 the source plane is located at infinity by effect of the collimation lens, its intermediate image is projected directly onto the common focal plane of the relay setup, which contains also the aperture stop of the objective. It is straighforward to find that onto this plane the irradiance distribution is given by

$$I_{stop}(\mathbf{x}) \propto I_S \left(\frac{-f_{TL1}\mathbf{x}}{f_c} \right) \otimes_2 \left[\delta \left(\mathbf{x} - \frac{\lambda_{ex} f_{TL1} M_{ill} \mathbf{u}_m}{2} \right) + \delta \left(\mathbf{x} + \frac{\lambda_{ex} f_{TL1} M_{ill} \mathbf{u}_m}{2} \right) \right] , \tag{15}$$

i.e., two replicas of a scaled version of the original source irradiance distribution $I_S(\mathbf{x})$. If these replicas are not clipped by the aperture stop of the objective, considered as the sole limiting

element of the relay system, further propagation of this distribution onto the sample space will result in Eq. (10), with no extra variation of the visibility of the projected 3D pattern. This outcome is clearly different from the behaviour of other projection schemes [10], in which the visibility of the illumination pattern is directly affected by the non-uniform OTF of the relay system.
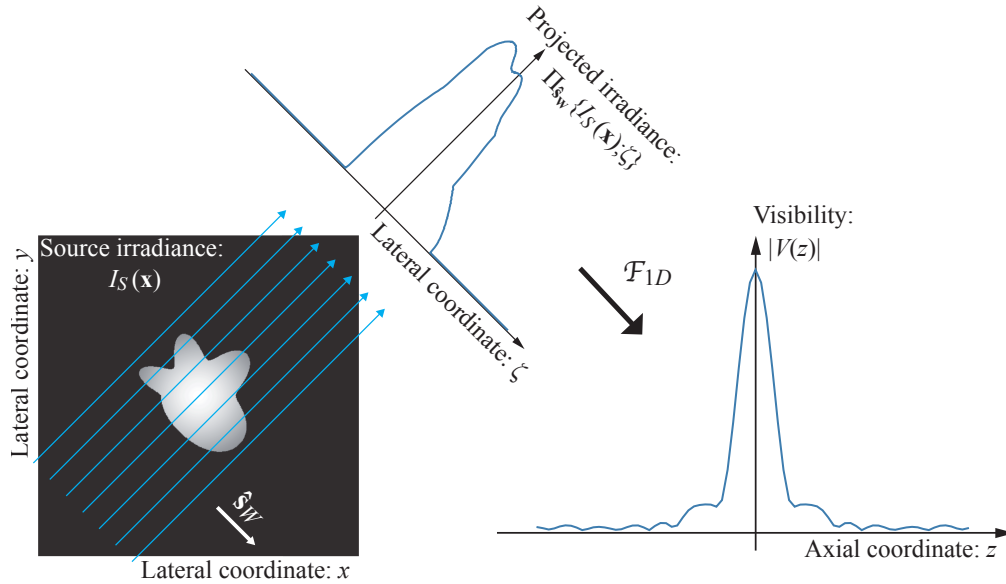

Fig. 3. Diagram of the procedure for obtaining the axial modulation of the visibility of the structured illumination with the proposed setup from the irradiance distribution $I_S(\mathbf{x})$ of the incoherent source, based on Eq. (13). The blue arrows represent line integrals (projection) and the symbol $\mathcal{F}_{1D}$ stands for a 1D Fourier transformation.

It is very interesting also to provide some physical insight on the coherence properties of the light field generated onto the aperture stop plane. Note that each point in the original source emits light completely incoherent with the radiation exiting any other point in the source. However, in the aperture stop plane each original point has been transformed into a perfectly coherent pair of point sources, each of these pairs remaining incoherent with the other ones. The final lateral modulation of the illumination in the sample space is caused by the interference between these paired sources, plus an incoherent superposition of these results for the whole set of pairs. On the other hand, each coherent pair has been symmetrically generated around the position of the original source point, following the direction $\hat{\mathbf{s}}_W$ fixed by the orientation of the Wollaston prism. In this way, clipping one of the replicas of the whole source that has been generated onto the aperture stop will leave some of the points on the other one unpaired. These set of unpaired points will produce no interference patterns, but a uniform background that will affect the visibility of the whole 3D pattern then obtained. This is, consequently, an adverse effect that should be avoided when the technique here presented is implemented.

2.2. Impact of the extended illuminating source on the synthetic SIM OTF and PSF

Let us now estimate the effective synthetic SIM OTF that relates the final reconstructed image and the original object. A convenient way for this estimation is following the classical analytical reconstruction procedure used in SIM, although the estimated effective OTF will be the same regardless of the reconstruction method that is used (for a review of SIM reconstruction methods see [5] and references therein). Conventional SIM algorithms are based on the use of multiple
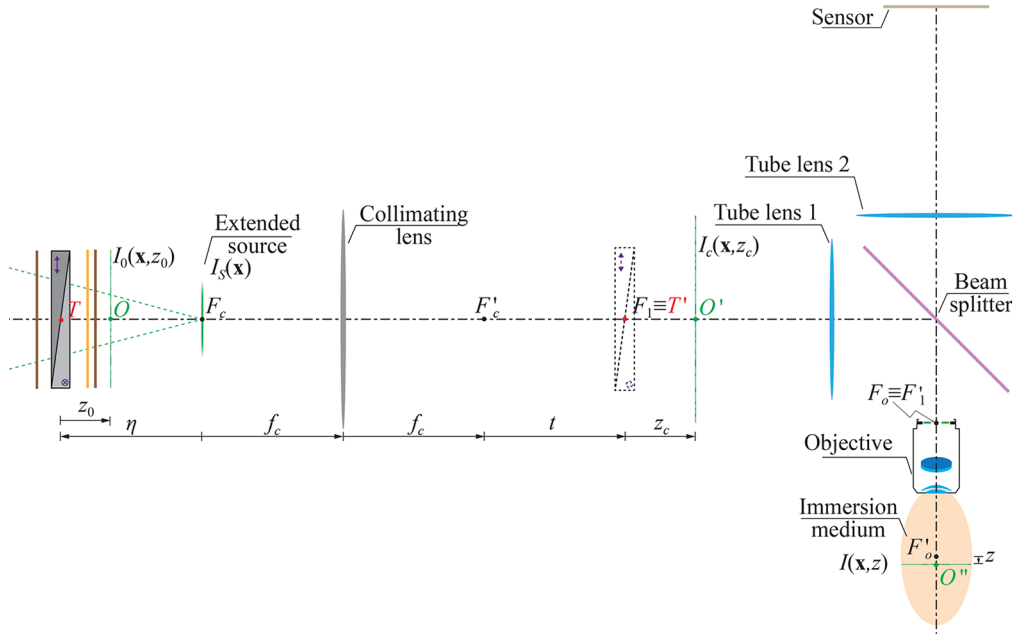
Fig. 4. Schematic or our TSIM experimental setup. A telecentric configuration in illumination is considered, where the respective front and back focal points of the tube lens 1 (F_1') and the objective (F_o) are coincident. An intermediate image of the extended source is, therefore, located at this plane.

forward images in which the SI pattern has been laterally shifted. The required number of images depends on the amount of lateral frequencies involved in the SI pattern. In our case, since a single lateral frequency $\mathbf{u}_m$ is used, only 3 raw images are needed in each orientation of the SI pattern. Thus, we assume three stacks of 2D images obtained after three phase shifts of the illumination pattern –$S(\mathbf{x}, z)$ in Eq. (10)– and subsequent axial scans of a 3D sample. If z_s is the axial displacement of the sample along the scanning process, then a raw image irradiance registered at the back focal plane of the tube lens in the collection (imaging) branch of the microscope is given by [3]

$$
I'_{TSIM}(\mathbf{x}, z_s; \phi) =
$$
$$
O\left(\frac{\mathbf{x}}{M}, \frac{z - M_z z_s}{M_z}\right) \left\{1 + \left|V\left(\frac{z}{M_z}\right)\right| \cos\left[2\pi \mathbf{u}_m \cdot \frac{\mathbf{x}}{M} + \phi + \Phi\left(\frac{z}{M_z}\right)\right]\right\} \otimes_3 h'(\mathbf{x}, z)\bigg|_{z=0}, \tag{16}
$$

where $O(\mathbf{x}, z)$ stands for the radiant exitance of the sample, ϕ is the lateral phase shift of the illumination pattern, $h'(\mathbf{x}, z)$ represents the irradiance PSF of the microscope in the image space, and M and M_z correspond to the lateral and axial magnifications of the imaging branch of the microscope, respectively. The symbol $\otimes_3$ is used here for the 3D convolution operation. This result can be expressed as

$$
\begin{aligned}
I'_{TSIM}(\mathbf{x}, z_s; \phi) =\ & O\left(\frac{\mathbf{x}}{M}, -z_s\right) \otimes_3 h'(\mathbf{x}, -M_z z_s) + \\
& \frac{1}{2} O\left(\frac{\mathbf{x}}{M}, -z_s\right) e^{i\left[2\pi \mathbf{u}_m \cdot \frac{\mathbf{x}}{M} + \phi\right]} \otimes_3 V^*(z_s) h'(\mathbf{x}, -M_z z_s) + \\
& \frac{1}{2} O\left(\frac{\mathbf{x}}{M}, -z_s\right) e^{-i\left[2\pi \mathbf{u}_m \cdot \frac{\mathbf{x}}{M} + \phi\right]} \otimes_3 V(z_s) h'(\mathbf{x}, -M_z z_s).
\end{aligned} \tag{17}
$$

By projecting this result into the sample space, it is finally obtained that

$$
\begin{aligned}
I_{TSIM}(\mathbf{x}, z_s; \phi) = I'_{TSIM}(M\mathbf{x}, -z_S; \phi) = {}& O(\mathbf{x}, z_s) \otimes_3 h(\mathbf{x}, z_s) + \\
& \frac{1}{2} O(\mathbf{x}, z_s) e^{i[2\pi\mathbf{u}_m \cdot \mathbf{x} + \phi]} \otimes_3 V(z_s) h(\mathbf{x}, z_s) + \\
& \frac{1}{2} O(\mathbf{x}, z_s) e^{-i[2\pi\mathbf{u}_m \cdot \mathbf{x} + \phi]} \otimes_3 V(-z_s) h(\mathbf{x}, z_s) ,
\end{aligned}
\tag{18}
$$

where the hermiticity of $V(z)$ has been applied, and $h(\mathbf{x}, z_s)$ stands for the PSF of the microscope in the object space, given by

$$
h(\mathbf{x}, z) = h'(M\mathbf{x}, M_z z) .
\tag{19}
$$

The reconstruction process is more easily understood when described in the Fourier domain. Thus, after Fourier transforming Eq. (18), the following result is obtained

$$
\tilde{I}_{TSIM}(\mathbf{u}, w; \phi) = \tilde{I}_0(\mathbf{u}, w) + \tilde{I}_{+1}(\mathbf{u}, w)e^{i\phi} + \tilde{I}_{-1}(\mathbf{u}, w)e^{-i\phi} ,
\tag{20}
$$

where the three *orders* of the Fourier transform of the raw data stack are given by

$$
\begin{aligned}
\tilde{I}_0(\mathbf{u}, w) &= \tilde{O}(\mathbf{u}, w)H(\mathbf{u}, w) , \\
\tilde{I}_{+1}(\mathbf{u}, w) &= \frac{1}{2}\tilde{O}(\mathbf{u} - \mathbf{u}_m, w) \left[\tilde{V}(w) \otimes_1 H(\mathbf{u}, w) \right] , \\
\tilde{I}_{-1}(\mathbf{u}, w) &= \frac{1}{2}\tilde{O}(\mathbf{u} + \mathbf{u}_m, w) \left[\tilde{V}(-w) \otimes_1 H(\mathbf{u}, w) \right] ,
\end{aligned}
\tag{21}
$$

$H(\mathbf{u}, w)$ being the OTF of the native microscope in the object space. The symbol $\otimes_1$ stands for the 1D convolution operation on the axial spatial frequency w, while $\tilde{O}(\mathbf{u}, w) = \mathcal{F}_{3D}\{O(\mathbf{x}, z); \mathbf{u}, w\}$ and $\tilde{V}(w) = \mathcal{F}_{1D}\{V(z); w\}$ are, respectively, the 3D and the 1D Fourier transforms of the object exitance and the visibility axial modulation of the illumination pattern. The three required forward images are obtained by changing ϕ in Eq. (10) to generate, for each spatial frequency $(\mathbf{u}, w)$, a solvable system of three linear equations. After solving this system, the three orders in Eq. (20) become available and a reconstruction of the object can be performed by the superposition

$$
\tilde{O}_{TSIM}(\mathbf{u}, w) = \tilde{I}_0(\mathbf{u}, w) + \tilde{I}_{+1}(\mathbf{u} + \mathbf{u}_m, w) + \tilde{I}_{-1}(\mathbf{u} - \mathbf{u}_m, w) = \tilde{O}(\mathbf{u}, w)H_{SIM}(\mathbf{u}, w) ,
\tag{22}
$$

where the effective synthetic OTF $H_{TSIM}(\mathbf{u}, w)$ is given by

$$
H_{TSIM}(\mathbf{u}, w) = H(\mathbf{u}, w) + \frac{1}{2}\tilde{V}(w) \otimes_1 H(\mathbf{u} + \mathbf{u}_m, w) + \frac{1}{2}\tilde{V}(-w) \otimes_1 H(\mathbf{u} - \mathbf{u}_m, w) .
\tag{23}
$$

It is worth to note that this synthetic OTF has a broader passband than the original one, $H(\mathbf{u}, w)$. First, the presence of the replicas of this function centered at lateral frequencies $\pm\mathbf{u}_m$ increase the lateral cutoff frequency of the effective SIM OTF. On the other hand, the 1D convolutions along w in the second and third summands in Eq. (23) broadens the final OTF's support in the axial frequency direction as well. Although the former of these two effects is common to many SIM techniques, the latter is a unique feature related in this proposal to the extension and shape of the incoherent source of illumination. In this sense, recalling Eq. (13), it is straightforward to obtain that the Fourier transform of the visibility function is equal to the projection (perpendicular to $\hat{\mathbf{s}}_W$, as indicated in Fig. 3) of the source irradiance, namely

$$
\tilde{V}(w) = \Pi_{\hat{\mathbf{s}}_W} \left\{ I_S(\mathbf{x}); \frac{nM_{ill}f_c w}{u_m} \right\} .
\tag{24}
$$

Finally, from Eqs. (22) and (23) it is easy to obtain the reconstructed object irradiance in the space domain

$$
O_{TSIM}(\mathbf{x}, z) = O(\mathbf{x}, z) \otimes_3 h_{TSIM}(\mathbf{x}, z) ,
\tag{25}
$$

where the effective PSF is given by

$$
h_{TSIM}(\mathbf{x}, z) = \{1 + |V(z)| \cos[2\pi\mathbf{u}_m \cdot \mathbf{x} - \Phi(z)]\} h(\mathbf{x}, z) .
\tag{26}
$$

3.   Results and discussion

In this section we present a set of results to validate the SIM technique proposed above. We consider the typical implementation of an epi-illumination architecture. The layout of the setup we used is presented in Fig. 4. The experimental implementation was performed by using a Wollaston prism with a deviation angle $\gamma = 2.5°$, an achromat as a collimating lens with $f_c = 100$ mm, a PlanApochromat 60×, high numerical aperture ($NA = 1.4$), oil immersion ($n = 1.515$) microscope objective by Nikon, and an achromatic doublet as an illumination tube lens with focal length $f_{TL1} = 150$ mm. With these elements, we obtained a projection magnification $M_{ill} = 0.022$. As for the incoherent source we generated an aerial image of a rotating diffuser illuminated by a laser spotlight (from a laser diode with wavelength $\lambda_{ex} = 405 \pm 5$ nm), thereby breaking the spatial coherence and obtaining the narrowband incoherent illumination required by the TSIM design. Ideally, a filtered LED source, which is already a spatially incoherent source could be used as long as the LED is bright enough [14,15]. Finally, the collection (imaging) part of the setup included a second tube lens with focal length $f_{TL2} = 400$ mm and a sCMOS camera with 6.45 μm×6.45 μm pixels (Hamamatsu ORCA-Flash4.0). All these experimental parameters were translated directly to the simulations presented in the sections that follow. In these simulations we consider a fluorescent sample, with an emission wavelength $\lambda_{em} = 530$ nm. For the above optical elements, the lateral and axial cutoff frequencies for the native WFM system are given, respectively, by

$$u_c = \frac{2\,NA}{\lambda_{em}} = 5.28\ \mu\text{m}^{-1}\ ,\quad w_c = \frac{n - \sqrt{n^2 - NA^2}}{\lambda_{em}} = 1.77\ \mu\text{m}^{-1}\ . \tag{27}$$

3.1.   Experimental verification of the visibility function

To validate our proposal, we first experimentally checked the relationship in Eq. (13), that relates the axial modulation of the visibility of the illumination pattern, $V(z)$, and the projection of the irradiance distribution of the source, $I_S(\mathbf{x})$. For this purpose, we measure experimentally the visibility of transverse irradiance patterns in the sample space by projecting them through the complete system in Fig. 4, when a transverse plane mirror is axially scanned through the focal region of the microscope objective. Note that in this setup, an axial shift of the mirror by an amount z_m from the focal plane of the objective, projects the transverse plane located at $z = 2z_m$ onto the sensor. An *XZ* section of the registered focal stack is shown in Fig. 5, and two of the 2D (*XY*) images captured with the camera within the focal stack. From each of these *XY* images, the experimental visibility, V_{exp}, of the pattern was assessed by estimating the power (spatial) spectrum at the modulating frequency $\mathbf{u}_m$ and the corresponding DC contribution. In this verification, the lateral frequency was set to $u_m = 0.80\ u_c$.

We investigated different illumination sources, and each case, an image of the actual source was captured. Since, as can be seen in Fig. 4, an intermediate image of the source is generated at the back focal plane of the microscope objetive (also the aperture stop plane), an additional lens was interleaved between the beam splitter and the second tube lens, acting as a kind of Bertrand lens. We used an achromat with focal length $f_B = 300$ mm for this purpose, and its position was tuned to project a sharp image of the aperture stop and the incoherent source onto the camera sensor. It is important to state here that the actual irradiance distribution of the source corresponded to a demagnified version of the image captured in this way. From the specifications used in the setup, this magnification was set to $M_B = f_{TL2}f_{TL1}/(f_B f_c) = 2$. In all cases, we oriented the Wollaston prism in such a way that the projection in Eq. (13) is performed along the vertical (*Y*) direction of the captured image of the source ($\hat{\mathbf{s}}_W$ parallel to the horizontal *X* axis).

Figure 6 shows the comparison of the results for three different sources, generated by projecting the same spot from the rotating diffuser into masks of different sizes. In the three cases it is clear that a good match is achieved between the experimental visibility V_{exp} and the Fourier transform
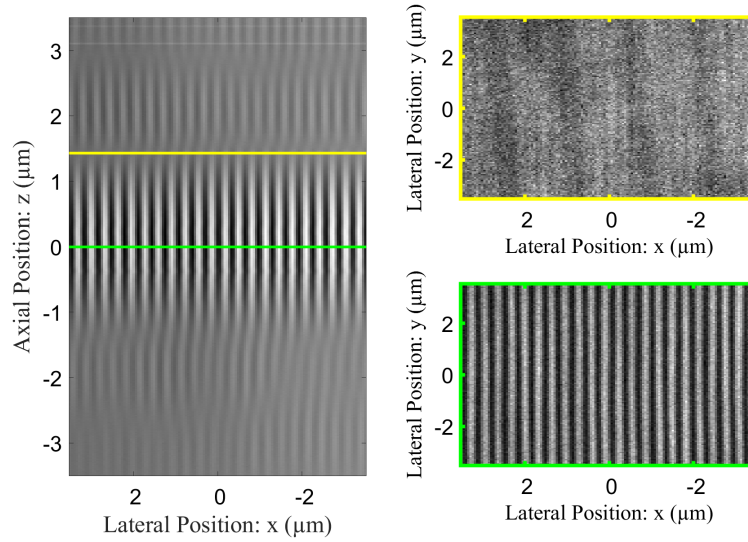
Fig. 5. 2D plots of the experimental illumination irradiance in the *XZ* plane in the sample space (left), and in *XY* planes for a position *z* with maximum (green) and zero visibility (yellow). The illumination was generated with a rectangular extended source by using a slit with width $L = 0.8$ mm, and it was measured by scanning a mirror sample.

of the projection of the source irradiance distribution $\Pi_{\hat{\mathbf{s}}_W} \{I_S(\mathbf{x}); \zeta\}$. Note that the differences can be explained as an undersampling effect of V_{exp}, since for the smaller source in Fig. 6(c) (which generates a slower axial variation of the visibility) we found the best agreement.

3.2. Assessment of the effective SIM OTF by numerical simulations

To assess the typical improvement that we can induce on the effective OTF of a SIM system with our illumination scheme, we simulate the expected results when using an ideal slit, oriented perpendicular to the characteristic vector $\hat{\mathbf{s}}_W$ of a Wollaston prism, as the effective incoherent source of the device. In practice, this shape can be tailored by an adjustable mask (or an electro-optical spatial light modulator for finer control) onto an aerial image of the actual source. In this case, we consider a source with an irradiance distribution given by

$$I_S(\mathbf{x}) = \frac{1}{lL}\text{rect}\left(\frac{x}{L}, \frac{y}{l}\right) \, , \tag{28}$$

rect(·) being the 2D rectangle function [20]. Note that for values of *l* much smaller than the diameter of the aperture stop of the microscope objective, the maximum value of *L* that avoids the clipping effect pointed in Section 2.1 is approximately given by (see Suplement 1)

$$L_{\max}(u_m) \simeq 2f_c \, NA \, M_{ill} \left(1 - \frac{\lambda_{ex}}{\lambda_{em}} \frac{u_m}{u_c}\right) \, . \tag{29}$$

The OTF of the original WFM setup in the sample domain is given by [21]

$$H(\mathbf{u}, w) = \frac{u_c}{2|\mathbf{u}|} \Re \left\{ \sqrt{1 - \left(\frac{|w|/w_c}{4|\mathbf{u}|/u_c} + \frac{|\mathbf{u}|}{u_c}\right)^2} \right\} \, , \tag{30}$$

where $\Re\{\cdot\}$ represents the real part of a complex number.
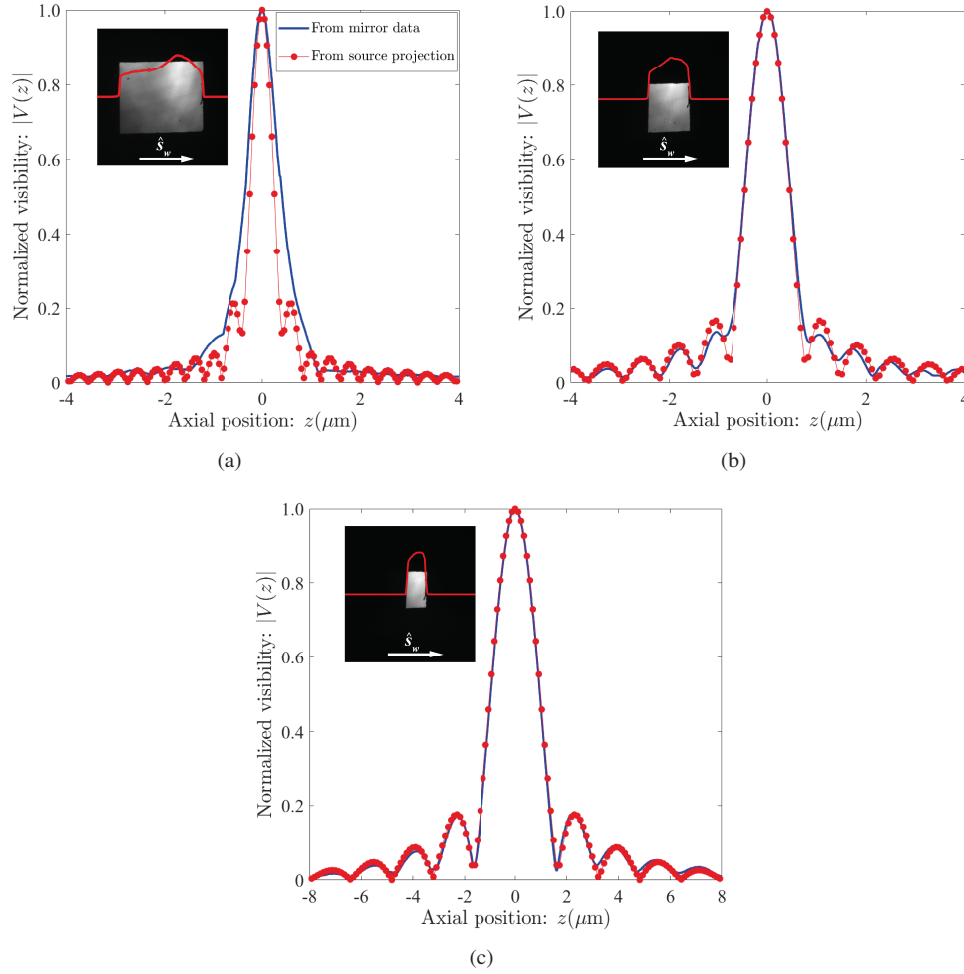
Fig. 6. Axial modulation of the visibility obtained by imaging a plane mirror (blue) and by Eq. (13) from the source irradiance distribution (red). The insets show images of the actual sources as registered by the camera, and their vertical projections (see Fig. 3) with widths equal to: (a) $L = 2.06$ mm; (b) $L = 1.01$ mm; and (c) $L = 0.56$ mm. The lateral frequency was set to $u_m = 0.80u_c$.

For comparison purposes, we consider two conventional approaches in SIM, namely, 2WSIM and 3WSIM. In the first case, for a given lateral modulation frequency $\mathbf{u}_m$ the effective final OTF is just constructed as

$$H_{2WSIM}(\mathbf{u}, w) = H(\mathbf{u}, w) + \frac{1}{2}H(\mathbf{u} + \mathbf{u}_m, w) + \frac{1}{2}H(\mathbf{u} - \mathbf{u}_m, w) \,, \tag{31}$$

while for the 3WSIM case it is straighforward to obtain

$$
\begin{aligned}
H_{3WSIM}(\mathbf{u}, w) = & H(\mathbf{u}, w) + \\
& \frac{1}{3} H\left(\mathbf{u} - \frac{\mathbf{u}_m}{2}, w + w_m\right) + \frac{1}{3} H\left(\mathbf{u} - \frac{\mathbf{u}_m}{2}, w - w_m\right) + \\
& \frac{1}{3} H\left(\mathbf{u} + \frac{\mathbf{u}_m}{2}, w + w_m\right) + \frac{1}{3} H\left(\mathbf{u} + \frac{\mathbf{u}_m}{2}, w - w_m\right) + \\
& \frac{1}{3} H(\mathbf{u} - \mathbf{u}_m, w) + \frac{1}{3} H(\mathbf{u} + \mathbf{u}_m, w) ,
\end{aligned}
\tag{32}
$$

where

$$
w_m = \frac{n - \sqrt{n^2 - \left(\frac{\lambda_{em} u_m}{2}\right)^2}}{\lambda_{em}} = \frac{n - \sqrt{n^2 - \left(NA \frac{u_m}{u_c}\right)^2}}{\lambda_{em}} .
\tag{33}
$$

Note that in both cases we have considered the same amplitude for the two/three waves involved in the generation of the illumination pattern. The functions in Eqs. (31) and (32) will be compared next with the effective final OTF provided by our proposal, as stated in Eqs. (23) and (24). As a general remark for next sections, it is interesting to recall that all the OTFs here considered have real and positive values, since we are considering a well-corrected, aberration-free microscope objective as the native element of the WFM configuration.
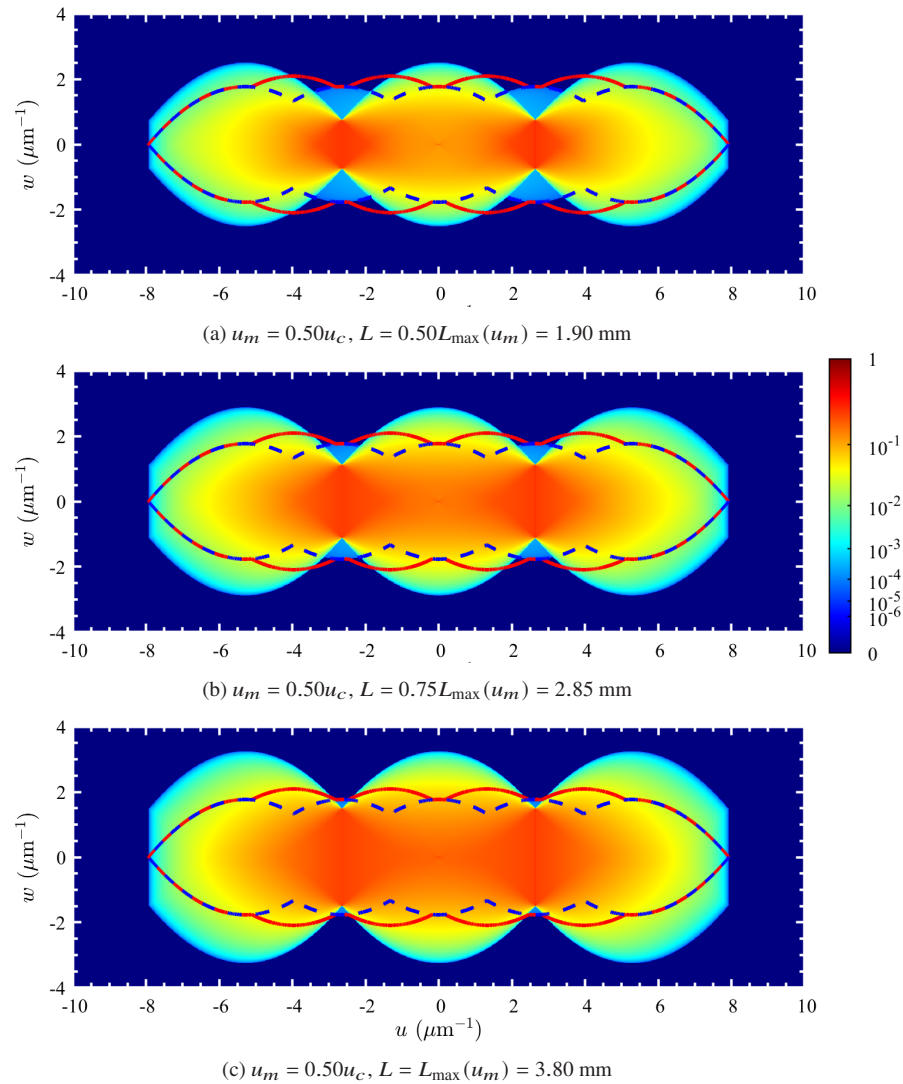
3.2.1. OTF compact support

To investigate how our proposed TSIM system compares to other SIM schemes we study their frequency response by focusing our attention in the coordinate plane with $\mathbf{u} = (u, 0)$ (cited as $u - w$ plane from now on). Figures 7–9 show a representation in the $u - w$ plane of $H_{TSIM}(\mathbf{u}, w)$, jointly with an overlay of the compact support border line of $H_{2WSIM}(\mathbf{u}, w)$ and $H_{3WSIM}(\mathbf{u}, w)$. In all cases, we display a normalized representation mapped to the same color scale. We present the results corresponding to three particular modulation frequencies, namely, $u_m = 0.50u_c$, $u_m = 0.75u_c$, and $u_m = 0.80u_c$. The first case corresponds to the best optical sectioning capability of the 2WSIM scheme while the latter is a practical limit of many current implementations of SIM. For our TSIM proposal, we display the results corresponding to three source widths for each modulation frequency: $L = 0.50L_{max}$, $L = 0.75L_{max}$, and $L = L_{max}$, where L_{max} is the largest source size that can be used for a given modulation frequency due to the clipping discussed earlier, as stated in Eq. (29). Note the dependende of this limit with the particular modulation frequency u_m implemented. Although it is clear that only a point by point comparison may establish the superiority of one of these OTF functions at a particular spatial frequency, we try next to give some global metrics for this assessment. First, we can see that the maximum extent (effective cutoff frequency) in the lateral direction is the same for the three cases, namely, $u_{max} = u_c + u_m$. On the other hand, only for the case of the smallest size of the source the axial cutoff values of the TSIM OTF are slightly lower than those in the 3WSIM case. In all the other situations, TSIM provides a larger effective axial cutoff frequency. In fact, it is straightforward from Eqs. (31), (32), and (23), to find that this effective axial cutoff frequency is given, for the 2WSIM, 3WSIM and TSIM setups, respectively, by

$$
w_{max,2W} = w_c ,
\tag{34}
$$

$$
w_{max,3W} = w_c + \frac{n - \sqrt{n^2 - \left(\frac{\lambda_{em} u_m}{2}\right)^2}}{\lambda_{em}} ,
\tag{35}
$$

$$
w_{max,T} = w_c + \frac{L u_m}{2 n M_{ill} f_c} .
\tag{36}
$$

(a) $u_m = 0.50 u_c$, $L = 0.50 L_{\max}(u_m) = 1.90$ mm

(b) $u_m = 0.50 u_c$, $L = 0.75 L_{\max}(u_m) = 2.85$ mm

(c) $u_m = 0.50 u_c$, $L = L_{\max}(u_m) = 3.80$ mm

Fig. 7. Meridional section ($u - w$ plane) of the 3D synthetic TSIM OTF for $u_m = 0.50 u_c$ and for three different rectangular source widths L. For better visualization, the OTF is normalized to 1. For the sake of comparison, the support border line of the OTFs for 2WSIM and 3WSIM are shown with a dashed navy blue line and with a solid red line, respectively.
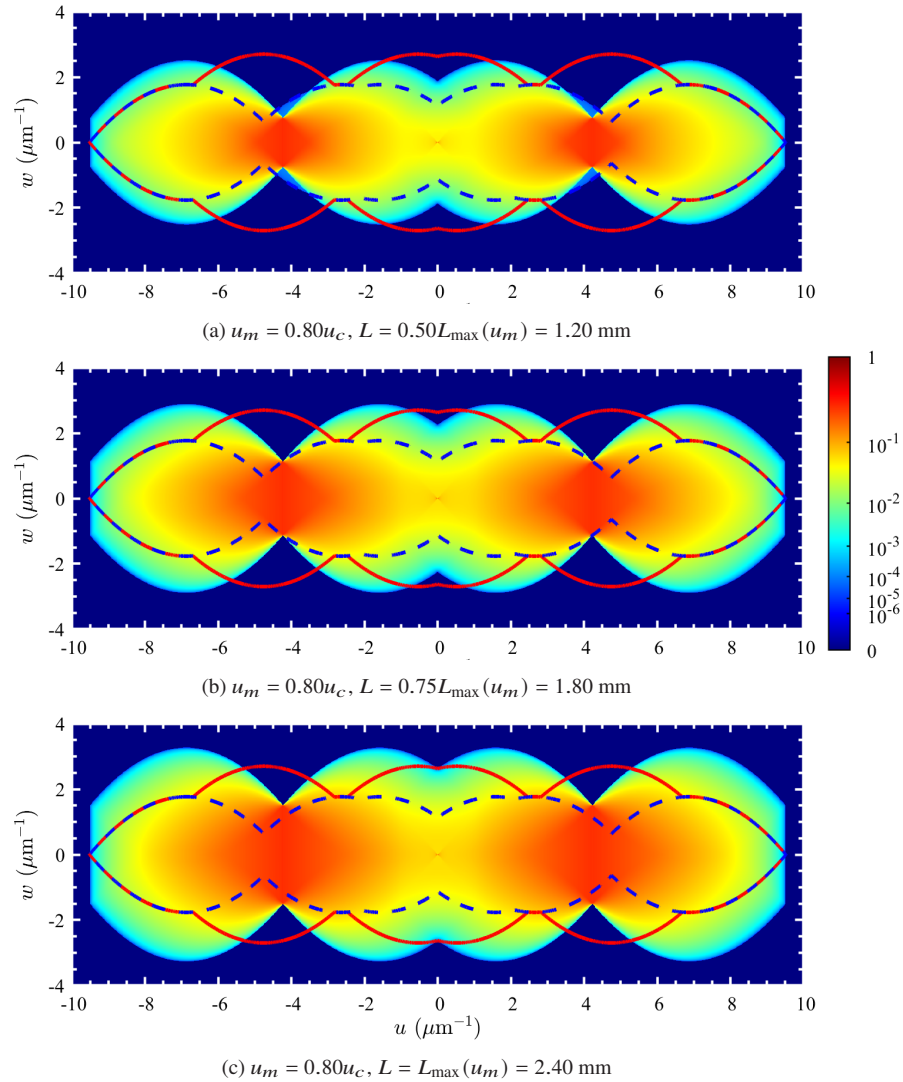
A plot of these effective axial cutoff frequencies for a continuous variation of the lateral modulation frequency u_m is shown in Fig. 10. From this figure it is clear that the best performace for the effective axial frequency is achieved for TSIM at $u_m = 0.65 u_c$, independently of the source width L. This maximum value is, for the optimal case $L = L_{\max}$, $w_{\max,T} = 1.90 w_c$ (green circle in the plot), that is quite bigger than the value attained by 3WSIM working at $u_m = 0.8 u_c$ ($w_{\max,3W} = 1.53 w_c$, red circle in the figure). Note also that $w_{\max,T}$ functions in Fig. 10 are quite flat around their maximum values: an effective axial cutoff frequency bigger than 90% of the peak value is attained within the interval $u_m \in (0.35 u_c, 0.95 u_c)$. In fact, only for modulation frequencies larger than $u_m = 0.92 u_c$ (see blue circle in Fig. 10), 3WSIM outperforms TSIM with
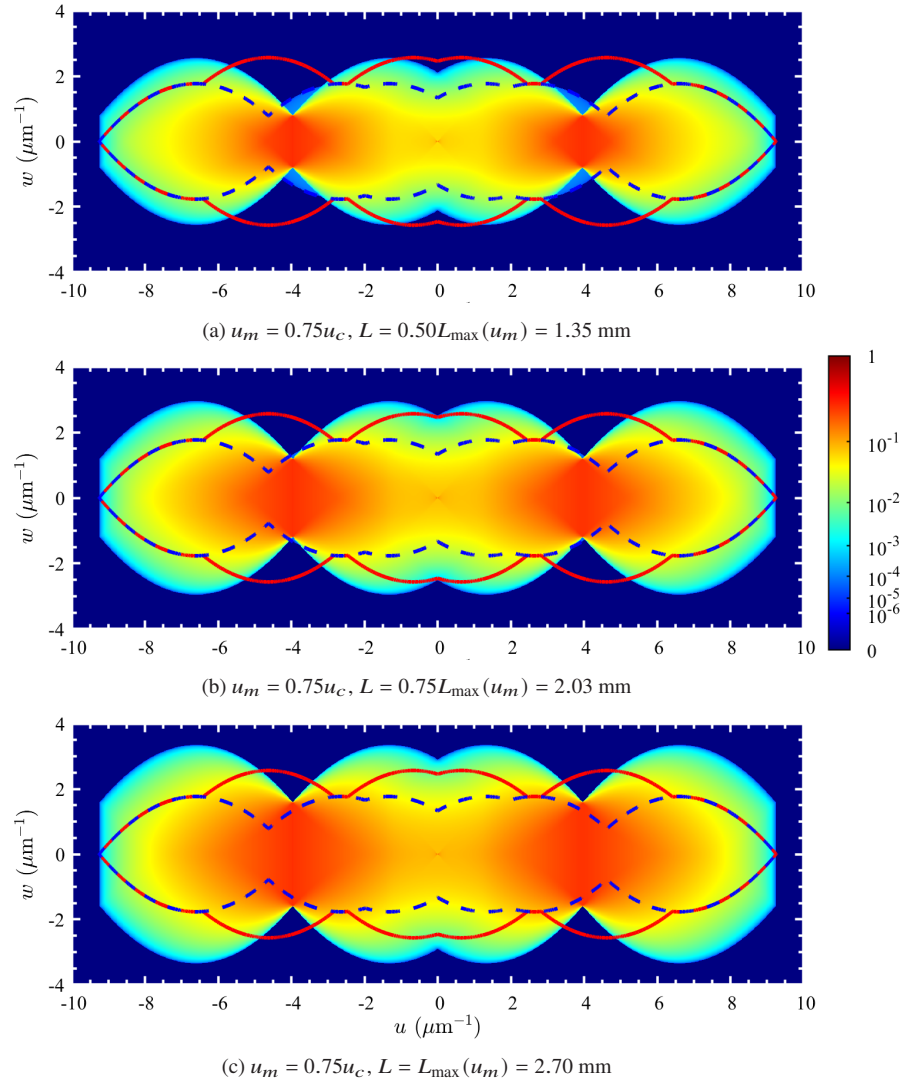
Fig. 8. Meridional section ($u - w$ plane) of the 3D synthetic TSIM OTF for $u_m = 0.75u_c$ and for three different rectangular source widths L. For better visualization, the OTF is normalized to 1. For the sake of comparison, the support border line of the OTFs for 2WSIM and 3WSIM are shown with a dashed navy blue line and with a solid red line, respectively.

$L = L_{\max}$. This range of frequencies is not achievable in practice for conventional SIM systems without compromising severely the final reconstruction performance.

On the other hand, if an ideally perfect filtering postprocessing is assumed, the area of the compact support of the OTFs can be considered as a measure of the potential coverage of the 3D sample's spectrum by the imaging system. Table 1 shows a measure of these areas for the situations under study, showing that the results provided by our proposal are better in all cases compared with 2WSIM. When compared with 3WSIM, all situations are favourable to our TSIM proposal, except for $u_m = 0.80u_c$ and $L = 0.50L_{max}$. In this particular case both 3WSIM and TSIM results differ less than 1%.

(a) $u_m = 0.80u_c$, $L = 0.50L_{\max}(u_m) = 1.20$ mm

(b) $u_m = 0.80u_c$, $L = 0.75L_{\max}(u_m) = 1.80$ mm

(c) $u_m = 0.80u_c$, $L = L_{\max}(u_m) = 2.40$ mm

Fig. 9. Meridional section ($u - w$ plane) of the 3D synthetic TSIM OTF for $u_m = 0.80u_c$ and for three different rectangular source widths L. For better visualization, the OTF is normalized to 1. For the sake of comparison, the support border line of the OTFs for 2WSIM and 3WSIM are shown with a dashed navy blue line and with a solid red line, respectively.

3.2.2. Axial OTF and integrated intensity

A part of the 3D OTF that has a particular practical interest is its profile along the $\mathbf{u} = \mathbf{0}$ line (referred to as axial OTF from now on). This function is relevant since it gives an assessment of the optical sectioning (OS) capability of the imaging system. In fact, its 1D Fourier transform represents the integrated intensity, a typical metric of OS. In Fig. 11 the axial OTFs for the three systems under comparison are shown, again for $u_m = 0.50u_c$, $u_m = 0.75u_c$, and $u_m = 0.80u_c$. The same set of values for the width L of the source is considered in the TSIM case. In all cases we have omitted the common spike-like contribution at $w = 0$ due to the central WFM OTF present in the three schemes under comparison. It is important here to recall that, as a rule of thumb, the narrower the axial OTF, the wider (worse) the integrated intensity. As displayed in
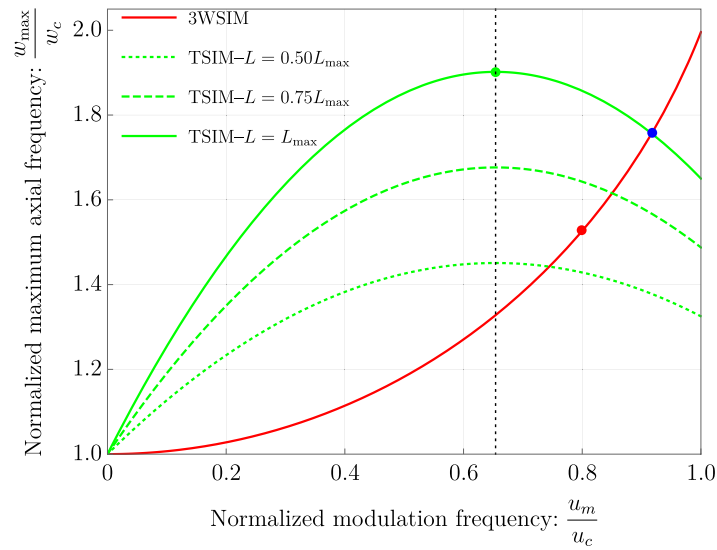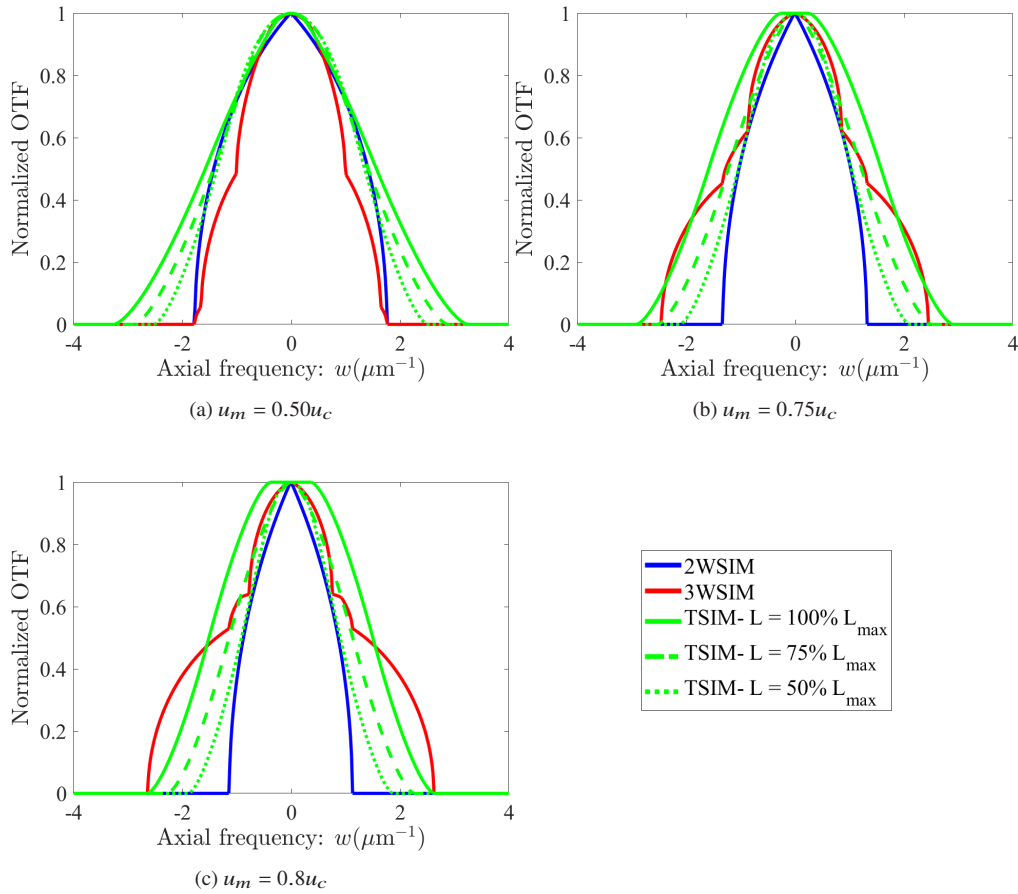
Fig. 10. Plot of the effective axial cutoff frequency w_{max} for 3WSIM (red) and our proposed TSIM (green) for different modulation frequencies u_m. The same three source widths L as above are considered here. The dashed line locates the modulation frequency ($u_m = 0.65u_c$) that provides the maximum achievable w_{max} for our proposal. 3WSIM outperforms TSIM only for modulation frequencies larger than $u_m = 0.92u_c$ (see blue circle).

Table 1. Areas of the compact support of the OTFs in the $u - w$ plane. All values have been normalized to the WFM OTF area in this same plane.

SIM architecture		Normalized area of the OTF's support		
		$u_m = 0.50u_c$	$u_m = 0.75u_c$	$u_m = 0.80u_c$
2WSIM		1.87	2.12	2.14
3WSIM		2.15	2.91	3.10
TSIM	$L = 0.50L_{max}$	2.58	3.04	3.07
	$L = 0.75L_{max}$	2.98	3.57	3.62
	$L = L_{max}$	3.41	4.14	4.20

Fig. 11, the extent of the axial OTF for TSIM is always bigger than for 2WSIM. As compared with 3WSIM, the extent of our proposal is similar in the case of maximum width of the source and slightly smaller for the rest. However, our proposals present higher values in some intervals of the support of the axial OTF.
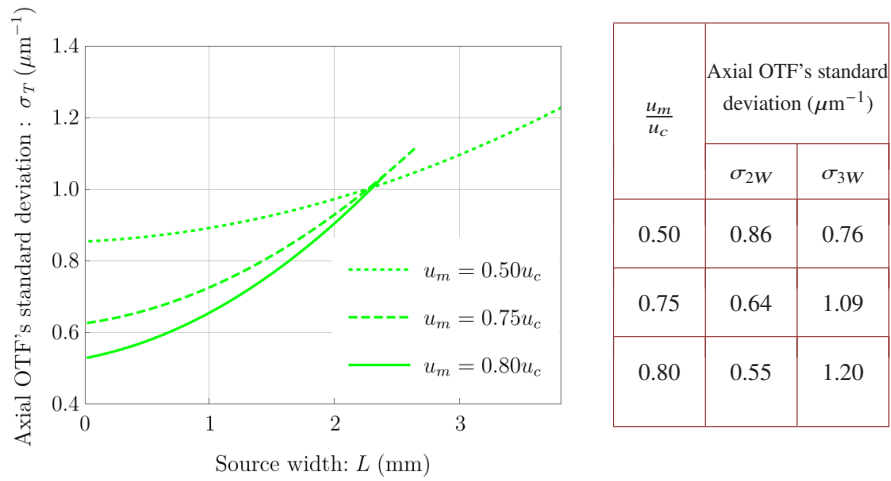
To estimate a more meaningful parameter related with the effective width of these functions, we show in Fig. 12 the standard deviation σ of these functions [22] for the three modulation frequencies under study and the whole continuous range of allowed widths L. The table on the right side of this figure shows the corresponding values of the standard deviations for 2WSIM (σ_{2W}) and 3WSIM (σ_{3W}) for the three frequencies under study. By comparing the values therein with Fig. 12, it is clear that our proposed system is always better than 2WSIM while only for the higher values of the width of the source TSIM competes with 3WSIM for $u_m = 0.50u_c$ and $u_m = 0.75u_c$. Although for $u_m = 0.8u_c$ the standard deviation value for the TSIM axial OTF does not reach the 3WSIM value for the higher modulation frequency, nevertheless it achieves an extreme value very close to it. Finally, we also computed the corresponding integrated intensities by Fourier transforming the axial OTF profiles. For the three situations plotted in Fig. 11, this

(a) $u_m = 0.50u_c$

(b) $u_m = 0.75u_c$

2WSIM
3WSIM
TSIM- L = 100% L$_{max}$
TSIM- L = 75% L$_{max}$
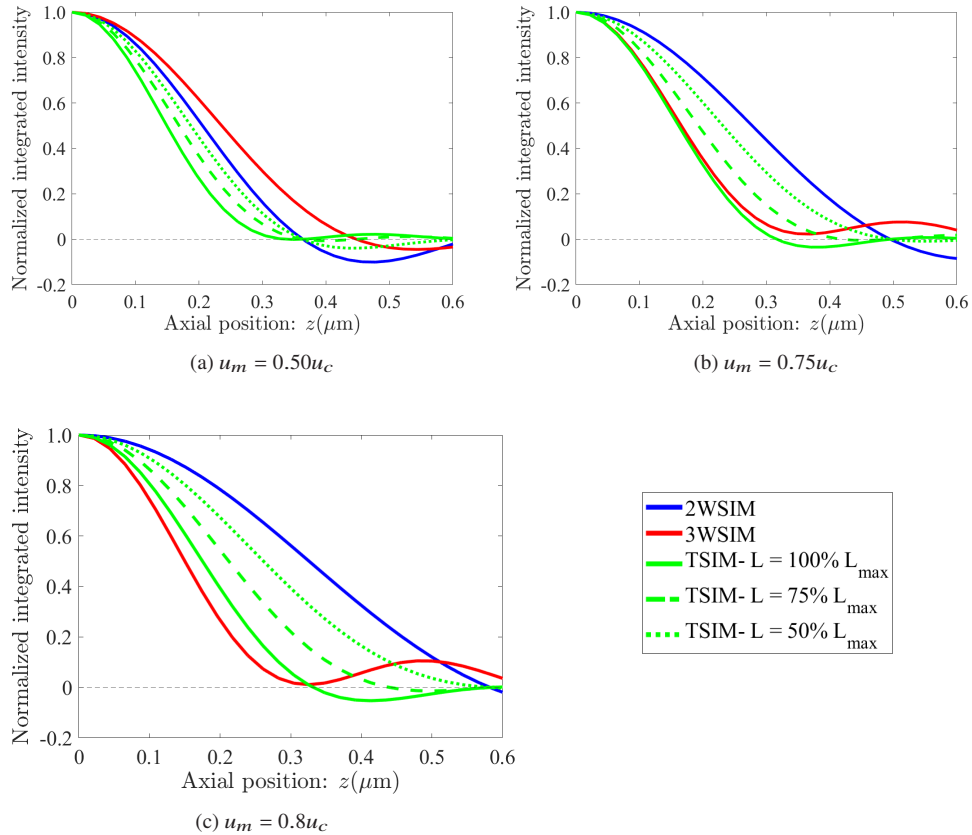TSIM- L = 50% L$_{max}$

(c) $u_m = 0.8u_c$

Fig. 11. Profiles of the axial OTF without the central WFM contribution, for 2WSIM (blue), 3WSIM (red) and our proposal (green) for a slit-like/rectangular source of three different widths *L*, and for three different modulation frequencies u_m.

operation leads to the graphs shown in Fig. 13. Note, again, that the common WFM constant contribution has not been considered in any case, and that the negative values obtained for the integrated intensities have to be considered as deviations from this common background. To estimate the width of these axial responses we evaluated the half-width at half-maximum (HWHM) for TSIM ($HWHM_T$), for the same range of values of the source width *L* as in Fig. 12. The final results are shown in Fig. 14, where the HWHM values for 2WSIM ($HWHM_{2W}$) and 3WSIM ($HWHM_{3W}$) have been included in a table as a reference for each modulation frequency **u**$_m$. Again, the comparison of the three architectures shows a better performance of TSIM compared with 2WSIM in all cases. When using 3WSIM as a reference, for the two lower modulation frequencies considered here, there are ranges of values of the width *L* that generate smaller HWHM in the integrated intensities for TSIM. For the higher frequency ($u_m = 0.80u_c$), TSIM underperforms as compared with 3WSIM. However, for the lower frequency ($u_m = 0.5u_c$), TSIM outperforms 3WSIM.

Anyway, as shown in all the results above, for a given modulation frequency u_m the best performance of our TSIM proposal happens with the biggest source possible. To complete the comparison of the three SIM schemes, in Fig. 15 we represent the result of the computation of the HWHM values of the integrated intensities (disregarding the constant backgroud from

| $\dfrac{u_m}{u_c}$	Axial OTF's standard deviation (μm^{-1})	
	σ_{2W}	σ_{3W}
0.50	0.86	0.76
0.75	0.64	1.09
0.80	0.55	1.20

Fig. 12. Plot of the standard deviation σ_T of the TSIM axial OTF without the WF delta-like contribution for our proposal with slit-like/rectangular sources of a range of different widths L and for three different modulation frequencies u_m. For comparison, standard deviation values obtained for 2WSIM (σ_{2W}) and 3WSIM (σ_{3W}) in the three cases under study are shown in the table on the right .

(a) $u_m = 0.50u_c$

(b) $u_m = 0.75u_c$

(c) $u_m = 0.8u_c$

Fig. 13. Plots of the integrated intensities without the WFM contribution, for 2WSIM (blue), 3WSIM (red) and our proposal (green) for a slit-like/rectangular source of three different widths L, and for three different modulation frequencies u_m.

$\frac{u_m}{u_c}$	Integrated intensity's HWHM (μm)	
	$HWHM_{2W}$	$HWHM_{3W}$
0.50	0.21	0.24
0.75	0.28	0.17
0.80	0.33	0.15
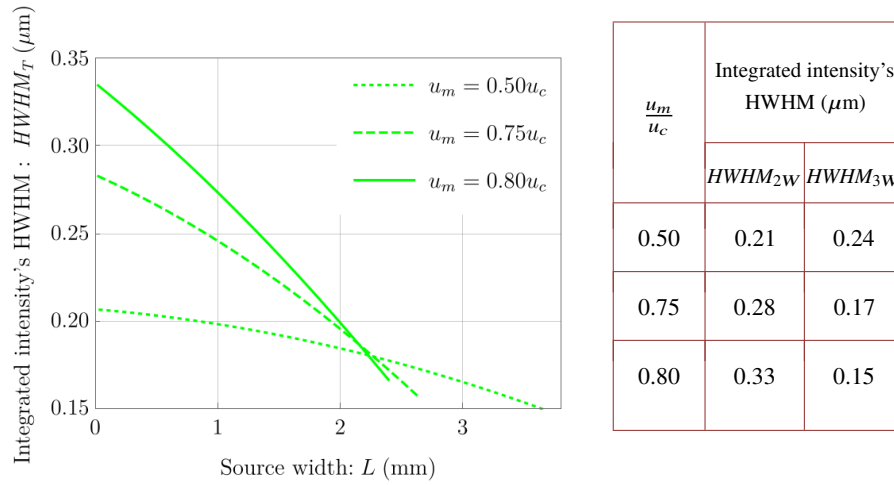
Fig. 14. Plot of the half-width at half-maximum $HWHM_T$ measured from the integrated intensity, after removing the WFM contribution (see Fig. 13), for our proposal with slit-like/rectangular sources of a range of different widths L and for three different modulation frequencies u_m. For comparison, half-width at half-maximum values obtained for 2WSIM ($HWHM_{2W}$) and 3WSIM ($HWHM_{3W}$) in the three cases under study are shown in the table on the right .
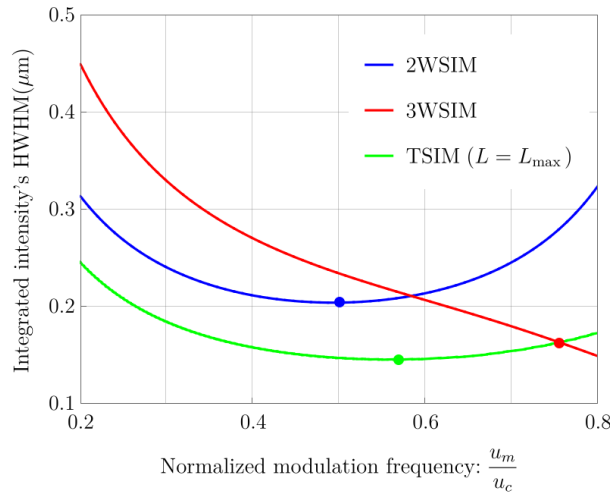
Fig. 15. Plot of the HWHM measured from the integrated intensities, after removing the WF contribution, for 2WSIM (blue), 3WSIM (red) and our proposed TSIM (green) for different modulation frequencies u_m. For each frequency TSIM is considered to work at its optimal configuration, i.e., using the biggest source posible.

the common WFM contribution) obtained for values of modulation frequencies ranging from $u_m = 0.2u_c$ and $u_m = 0.8u_c$ when the optimal situation $L = L_{\max}(u_m)$ is considered in the TSIM case. It is clear from this graph that, in its optimal configuration for each modulation frequency, TSIM outperforms the other two architectures for frequencies up to $u_m = 0.76u_c$. This frequency defines the crossing point (in red) of the TSIM and 3WSIM curves in the graph, corresponding to a common value of the HWHM of 0.16μm. With regards to 2WSIM, it is also interesting to point out that this improved performance is extended to the whole range of possible source widths and

also that the minimum HWHM achieved is much smaller in the case of TSIM (see blue and green points in Fig. 15, corresponding to coordinates $(0.50, 0.21 \mu m)$ and $(0.57, 0.15 \mu m)$, respectively).

4. Conclusions

In this work, a 3D tunable SIM (TSIM) system based on a quasi-monochromatic extended source illuminating a Wollaston prism was presented, investigated and compared to two conventional approaches in SIM, namely 2WSIM and 3WSIM. The 3D illumination pattern of the TSIM system is axially varying while it simultaneously has lateral periodic variations, which can be tuned by simply axially displacing the Wollaston prism. The axial modulation of the visibility of the SI pattern is related to the 1D Fourier transform of the projection of the extended source, and it can be controlled by choosing the shape and the size of the source. Note that, although we only showed rectangular sources of different sizes in this paper, different source shapes can add an extra degree of freedom in the engineering of the axial modulation of the SI pattern.

Results from experimental verification of the axial visibility function demonstrate the validity of this relationship, which facilitates the determination of the visibility function by simply recording an image of the source at the back focal plane of the microscope objective lens. This direct knowledge of the actual visibility of the SI pattern provides a more realistic characterization of the system's OTF, which is needed for the reconstruction of the 3D sample.

Investigation of the engineered TSIM OTF, obtained by tuning the system's lateral modulation and the size of the source, shows that the area of the compact support of the OTF and its effective cutoff frequencies (which relate to the achieved super resolution) increase with an increase in the source size. For a given lens and lateral modulation frequency, there is a limit on the size of the source that can be used in practice (to avoid the clipping effect discussed in Section 2.2).

Our comparative study shows that as expected, the TSIM outperforms the 2WSIM system, because it offers axial modulation, while it offers desirable advantages over the 3WSIM under certain conditions. First, TSIM provides a larger axial cutoff frequency than 3WSIM in all investigated cases, and thus the expected achieved axial super resolution is better. It is also worth pointing out that the axial effective cutoff frequency for 3WSIM drops monotonically very fast as the modulation frequency decreases. Just a 10% decrease from the maximum theoretical value $u_m = u_c$ (which potentially would provide an effective axial cutoff frequency equal to $2w_c$) leads to a value $w_{\max,3W} = 1.72w_c$. On the other hand, in TSIM up to 1.9× improvement in axial resolution is achievable, but with lower lateral modulation frequencies (see Fig. 10). Thus, when high values of u_m are prevented or incovenient, TSIM provides a better axial performance than 3WSIM.

Second, assessment of the axial OTF and the integrated intensity, which provide a metric for the optical sectioning capability of the system, shows that TSIM outperforms the other two architectures for frequencies up to $u_m = 0.76u_c$.

Additional advantages of the presented TSIM system are the independent tunability of the achieved lateral and axial resolution, by tuning the lateral modulation frequency and the source size, respectively. This is not possible in 3WSIM were the lateral and axial modulation frequencies are non-linearly coupled, as shown in Eq. (33). Finally, our proposed system achieves a 40% data reduction compared to a standard 3WSIM system since only three phase-shifted images are needed per orientation of the pattern, as opposed to the five images required by the three-wave interference scheme. Future work will also comparatively investigate the impact of noise on 3D-SIM system performance , the use of the TSIM system to image calibration and biological samples and verify its performance through the reconstruction process.

Disclosures. The authors declare no conflicts of interest.

Data Availability. Data underlying the results presented in this paper are not publicly available at this time but may be obtained from the authors upon reasonable request.

Supplemental document. See Supplement 1 for supporting content.

References

1. M. G. L. Gustafsson, "Surpassing the lateral resolution limit by a factor of two using structured illumination microscopy," J. Microsc. **198**(2), 82–87 (2000).
2. M. G. L. Gustafsson, L. Shao, P. M. Carlton, C. J. R. Wang, I. N. Golubovskaya, W. Z. Cande, D. A. Agard, and J. W. Sedat, "Three-dimensional resolution doubling in wide-field fluorescence microscopy by structured illumination," Biophys. J. **94**(12), 4957–4970 (2008).
3. M. Martínez-Corral and G. Saavedra, "The Resolution Challenge in 3D Optical Microscopy," Prog. Opt. **53**, 1–67 (2009).
4. H. Shabani, A. Doblas, G. Saavedra, E. Sanchez-Ortiga, and C. Preza, "Improvement of two-dimensional structured illumination microscopy with an incoherent illumination pattern of tunable frequency," Appl. Opt. **57**(7), B92–B101 (2018).
5. C. T. S. Van and C. Preza, "Improved resolution in 3D structured illumination microscopy using 3D model-based restoration with positivity-constraint," Biomed. Opt. Express **12**(12), 7717–7731 (2021).
6. R. Heintzmann, "Saturated patterned excitation microscopy with two-dimensional excitation patterns," Micron **34**(6-7), 283–291 (2003).
7. E. Betzig, "Excitation strategies for optical lattice microscopy," Opt. Express **13**(8), 3021–3036 (2005).
8. M. Schropp and R. Uhl, "Two-dimensional structured illumination microscopy," J. Microsc. **256**(1), 23–36 (2014).
9. C. Zhang, N. Xu, and Q. Tan, "Compact structured illumination microscopy with high spatial frequency diffractive lattice patterns," Biomed. Opt. Express **13**(11), 6113–6123 (2022).
10. M. A. A. Neil, R. Juškaitis, and T. Wilson, "Method of obtaining optical sectioning by using structured light in a conventional microscope," Opt. Lett. **22**(24), 1905–1907 (1997).
11. A. Doblas, H. Shabani, G. Saavedra, and C. Preza, "Tunable-frequency three-dimensional structured illumination microscopy with reduced data-acquisition," Opt. Express **26**(23), 30476–30491 (2018).
12. H. Shabani, A. Doblas, G. Saavedra, and C. Preza, "Optical transfer function engineering for a tunable 3D structured illumination microscope," Opt. Lett. **44**(7), 1560–1563 (2019).
13. A. Doblas, H. Shabani, G. Saavedra, and C. Preza, "Comparison of 3D structured patterns with tunable frequency for use in structured illumination microscopy," Proc. SPIE **10070**, 100700H (2017).
14. S. Bedoya, A. Doblas, G. Saavedra, and C. Preza, "Tunable structured illumination system based on a Wollaston prism," *Imaging and Applied Optics 2018 OSA Technical Digest*, paper ITu2B.3 (2018).
15. A. Doblas, S. Bedoya, and C. Preza, "Wollaston prism-based structured illumination microscope with tunable frequency," Appl. Opt. **58**(7), B1–B8 (2019).
16. J. Sola-Pikabea, A. Doblas, G. Saavedra, M. Martinez-Corral, and C. Preza, "Optimal design of incoherent tunable-frequency structured illumination microscope scheme," *2018 IEEE 15th International Symposium on Biomedical Imaging*, 449–452 (2018). doi: 10.1109/ISBI.2018.8363613.
17. J. C. Barreiro, P. Andres, J. Ojeda-Casta neda, and J. Lancis, "Multiple incoherent 2D optical correlator," Opt. Commun. **84**(5-6), 237–241 (1991).
18. R. S. Longhurst, *Geometrical and Physical Optics* (Longman, New York, 1973).
19. R. Bracewell, "The Projection-Slice Theorem," in *Fourier Analysis and Imaging* (Springer, Boston, 2003).
20. J. D. Gaskill, *Linear Systems, Fourier Transforms, and Optics* (John Wiley & Sons, New York, 2005).
21. M. Gu, *Advanced Optical Imaging Theory* (Springer-Verlag, Berlin, 1999).
22. J. F. Kenney and E. S. Keeping, "The Standard Deviation," in *Mathematics of Statistics, Pt. 1* (Van Nostrand, Princeton, 1962).